Volume conductor models for magnetospinography

George C. O'Neill[a✉], Meaghan E. Spedden[b], Maike Schmidt[b], Stephanie Mellor[b,c,d], Matti Stenroos[e], Gareth R. Barnes[b]

[a]Department for Neuroscience, Physiology and Pharmacology, University College London, London, UK
[b]Department of Imaging Neuroscience, UCL Queen Square Institute of Neurology, University College London, London, UK
[c]Spinal Cord Injury Center, Balgrist University Hospital, Zürich, Switzerland
[d]Translational Neuromodeling Unit (TNU), Institute for Biomedical Engineering, University of Zurich & ETH Zurich, Zürich, Switzerland
[e]Department of Neuroscience and Biomedical Engineering, Aalto University School of Science, Espoo, Finland
✉g.o'neill@ucl.ac.uk

Abstract

The recent development of small, wearable, magnetic field sensors allow for the investigation of biomagnetic fields with a flexibility previously unavailable. We test models to describe how current flow in the spinal cord and thorax gives rise to measurable magnetic fields outside the torso. We compare various open-access volume conductor models, in order to select the most parsimonious and accurate descriptor of the magnetic fields due to source current in the spinal cord.

We find that fields produced due to current flow along the superior-inferior axis of the cord are relatively insensitive to the choice of volume conductor model. However, fields produced by current flow in predominantly left-right or anterior-posterior direction are significantly attenuated by the presence of bone in the forward model. Furthermore, volume conductors with bone demonstrate larger differences in field topographies for nearby sources compared to bone-free models. These findings suggest that precise modelling of spinal cord location and surrounding vertebrae will be important a-priori knowledge going forward.

---

1) Introduction

The spinal cord and its associated activity in sensorimotor networks are of interest to both basic neuroscience and clinical research. From a neuroscience perspective, understanding its integrative role in combining ascending afferent activity from the body to fine-tune descending motor control is an area of interest for researchers (Nielsen, 2016, 2004; Umeda et al., 2022). Whilst in the clinic it is desirable to non-invasively identify the location and severity of spinal cord injury (Stroman et al., 2014) and track any potential recovery from treatment approaches (Rejc et al., 2017; Shackleton et al., 2023).

One approach to measure activity originating from the spinal cord which is being developed is magnetospinography (MSG), where the activity is measured non-invasively from the magnetic fields generated by currents due to the neuronal activity. The potential advantages of using the magnetic field to measure spinal cord activity are twofold. First, the magnetic fields can be sensed without direct contact to the subject, avoiding the need for electrodes placed on the skin or invasively in the epidural space (Imajo et al., 2021; Prestor et al., 1991). Second, magnetic fields originating from neural activity are less affected by the poorly conducting bone than the corresponding electric potential, and overall the uncertainty of conductivity values of tissues affect magnetic signals less than electric signals, making modeling easier (Stenroos and Nummenmaa, 2016; Vorwerk et al., 2014). Therefore, if we were to localise where in the spinal cord these signals originated from, we should have an improved spatial resolution compared to the non-invasive measures based on electric potential (e.g. electrospinography; Chander et al., 2022; Steele et al., 2024).

Measuring magnetic fields from the spinal cord is a challenge due to its depth (~50 mm) from the skin surface and the relative low amplitude of the expected current moment (~10 nAm; Adachi and Kawabata, 2024). Quantum sensors with femtoTesla level sensitivity are required for this task and so initial research into MSG recordings have been performed using bespoke Superconducting Quantum Interference Devices (SQUIDs) systems (Adachi and Kawabata, 2024; Akaza et al., 2021; Hashimoto et al., 2022; Kawabata et al., 2002; Sumiya et al., 2017). These systems generate high quality data which can localise the spatiotemporal properties of the neuronal activity, but the bulky cryogenic support infrastructure means it can only image a limited portion of the spinal cord per experiment (Hashimoto et al., 2022). Recent advances in cryogen-free sensors (such as optically pumped magnetometers; OPMs) allow us similar sensitivity but with sensors the size of a 2x4 LEGO brick which can be flexibly placed anywhere near or on the back, allowing for the possibility of covering large areas of the back with OPMs and any other location relevant for measuring the peripheral nervous system. To this end, the first experiments with OPMs to measure spinal activity are coming online (Mardell et al., 2024; Spedden et al., 2024).

Irrespective of acquisition method, to fully leverage the source localisation abilities promised by MSG, we need to ensure we are approaching the forward problem (modelling how a known source current distribution is represented at the sensor-level) and inverse problem (estimating the current distribution from set of sensor-level observations) in a manner appropriate for the spinal cord. Previous source analyses of MSG data have used simple volume conductive models to solve the forward problem, such as assuming an infinite homogenous medium (Sumiya et al., 2017) or a basic approximation of the torso shape (Mardell et al., 2024).

This paper compares and contrasts a set of existing volume conductor modelling approaches from the magnetoencephalography (MEG) and magnetocardiography (MCG) literature, implemented in academic software toolboxes on a theoretical OP-MSG setup, to investigate the similarities and differences between them in the context of magnetospinography. Similar to previous

encephalographic conductive model comparison studies (Cao et al., 2022; Stenroos et al., 2014; Vorwerk et al., 2014), we test and compare increasingly complex volume conductors to understand the benefits additional modelling provides. Based on the results presented here, we make some recommendations on selecting an appropriate volume conductor for MSG.

2) Methods

2.1 Model geometry and source space

Our simulations are based on the anatomy and posture of a participant who undertook a previous OP-MSG study (Mardell et al., 2024). A scan of the particpant's head and torso whilst they were seated was generated using an infra-red structural camera (Occipital Inc, Boulder, CO). The geometry is shown in Figure 1A. To generate a basic boundary of the torso, we modified the thorax mesh provided in ECGsim (Oosterom and Oostendorp, 2004). First, we upsampled the ECGsim thorax, cardiac blood and lung meshes. Then, we included an abdomen and neck to for a new torso mesh and registered the mesh to the participant scan with a two-step process: an initial 7 degrees of freedom (translation, rotation and global scaling) fit using three fiducial locations, the left and right acromion, and L5 point of the spine was followed by a constrained iterative closest point fit to generate the full 12 degrees of freedom affine transformation. An cartoon example of this fit can be seen in Figure 1E. This transformation was also applied to the heart and lung meshes from ECGsim.

With the torso mesh fitted, we approximated the curvature of the spinal cord using a 5th order polynomial function and a source space was generated 50 mm deep with elementary sources placed 10 mm apart (see red dots in Figure 1A). For every elementary source (labelled as the medial source in Figure 1B), 8 other source locations, were placed to form a ring with 4 mm radius around the medial source (Figure 1B). This ring of sources was allowed to rotate along the plane of the ring to follow the curvature of the spine. Having generated a source space for the spinal cord, we also generated two additional meshes to represent the spinal cord conductive volume which wrapped the spinal cord with an 8 mm radius from the medial sources, and a second larger mesh representing the vertebrae with a radius of 16 mm from the medial sources. (see Figure 1G for an example). The median distance between vertices for the spinal cord and vertebrae meshes were 2.8 mm and 5.1 mm respectively.

Sensor locations were generated using a 2D grid of sensors (spaced 30 mm apart) which were then ray-cast onto the structural scan of the participant, keeping only the sensors which would also ray-cast with the fitted torso mesh. Sensors were placed 10 mm from the structural scan surface, which is approximately the distance the sensors are from the scalp in OP-MEG experiments (O'Neill et al., 2023; Rhodes et al., 2023). This generated 250 sensors (black dots in Figure 1A). The sensors were oriented such that their primary axis was along sagittal axis of the body, and tangential fields were measured along the frontal and transverse axes for a total of 750 channels. Triaxial measurements were chosen as both SQUID-based and OPM-based magnetospinographs already offer multi-axis recordings (Adachi and Kawabata, 2024; Mardell et al., 2024). The sensors were modelled point-like, i.e. the extent of the sensor was not accounted for in the model.

2.2 Volume conductor models

We investigated 11 different forward models that incorporate different approaches to volume conductor modelling, or different levels of conductor detail. Below we list the different models and preparation methods based on the increasing complexity. In all models, we define the sources in

terms of primary current distribution that is discretized into a set of elementary current dipoles. This source modelling approach enables the implementation of dipole scanning or multipolar sources if required.

2.2.1 Infinite homogeneous medium

The simplest volume conductor model is an infinite homogeneous conductor (Figure 1C). In this case, the ohmic currents (a.k.a. secondary currents) driven by the electric field do not contribute to the magnetic field, and thus only the field due to the primary current needs to be considered (Sarvas, 1987). The model is invariant to the conductivity of the medium. Effectively, we only need to calculate the magnetic field of the current dipole.

2.2.2 Spherically-symmetric medium

The sphere model is the simplest model that requires some geometrical information. In MEG the head can be approximated as a sphere (Sarvas, 1987), especially around the motor and somatosensory cortex (Stenroos et al., 2014). In this approach, all sources are assumed to be within a spherically symmetric volume conductor, and all sensors outside of it. Here the only hyperparameter we need to select (either explicitly of derived from fitting a sphere) is the sphere's origin; the radius is not needed. We set the origin approximately 1000 mm in front of the participant so that the sphere's surface approximated the curvature of the spine (which we denote as the Large Sphere; Figure 1D).

2.2.3 Corrected Sphere

Sometimes known in the encephalographic literature as Single Shell, the Corrected Sphere (Nolte, 2003) is also a popular volume conductor model in MEG for its ability to approximate the realistically-shaped skull geometry without the need for element calculations. Simply put, the spherically-symmetric solution is perturbed to better resemble the geometry it is trying to approximate. In this case it is done using the gradients of a spherical harmonic basis set. Here, we placed the origin of the sphere within the torso boundary and fitted spherical harmonic gradients up to an order of ℓ=10. The conductive boundary used to fit the spherical harmonic gradients can be found in Figure 1E. In MEG, the Corrected Sphere model performs as well as single compartment models solved with, for example, boundary element methods (Stenroos et al., 2014).

2.2.4 Boundary Element Models (BEMs)

In Boundary Element Models, one assumes a piecewise homogeneous conductivity profile. Here, we numerically solve for so-called secondary currents on the interfaces between surfaces where the conductivity of the tissue changes (i.e. on the boundaries), and compute both the primary and secondary magnetic fields. We tested 5 different variants of conductivity distributions, primarily by increasing the number of different tissue types. The 1c BEM (Figure 1E) incorporates just the torso volume; it should be roughly equivalent to the corrected sphere model. The 3c BEM also included the heart and lung meshes (Figure 1F); the 4c BEM included the spinal cord mesh; and the 5c BEM also included the bone mesh (Figure 1G). Having sources close to strong jumps of conductivity may lead to numerical issues that are alleviated by the Isolated Source Approach (Hamalainen and Sarvas, 1989; Stenroos and Sarvas, 2012). We tested the effect of isolation at the inner boundary of the spinal cord, resulting in 5ci BEM. The conductivities of each of the tissue types are as follows: 0.33 Sm^{-1} for the spinal cord, 0.007 Sm^{-1} for the bone, 0.62 Sm^{-1} for the heart, 0.05 Sm^{-1} for the lungs and 0.23 Sm^{-1} for the torso. We applied two different approaches to solve for the potentials on the surfaces. First we

used the linear collocation method via the Helsinki BEM Framework[1] (Stenroos et al., 2007; Stenroos and Nummenmaa, 2016), for all models from the 1c BEM to 5c BEM, and a linear Galerkin approach (Stenroos and Sarvas, 2012) for the 5c BEM models. The four BEM solvers in the text are denoted LC (linear collocation), LG (linear Galerkin) and LCi, LGi to represent variants with the isolated source approach included.

2.2.5 Finite Element Model (FEM)

The finite element modelling is the most computationally intensive approach, involving representing the whole volume conductor in terms of volume elements that each can have its own conductivity value. Here we took the surface meshes used in BEM and converted them into a single tetrahedral mesh with the ISO2MESH toolbox to prepare them for finite element analysis, with the constraint that no single tetrahedron could be any larger than 10 ml in volume. We considered the conductivity values to be homogeneous within each tetrahedron and their corresponding conductivity values were the same as for the BEM; in other words, we implemented a piecewise-homogeneous volume conductor model. The FEM was solved using the DuNeuro library (Schrader et al., 2021), in particular using the binaries compiled for the Brainstorm software suite (Medani et al., 2023). We used the Continuous Galerkin method with a St. Venant source model to represent the dipoles. Note we have ensured all sources are inside the spinal cord domain.

[1] https://github.com/MattiStenroos/hbf_lc_p

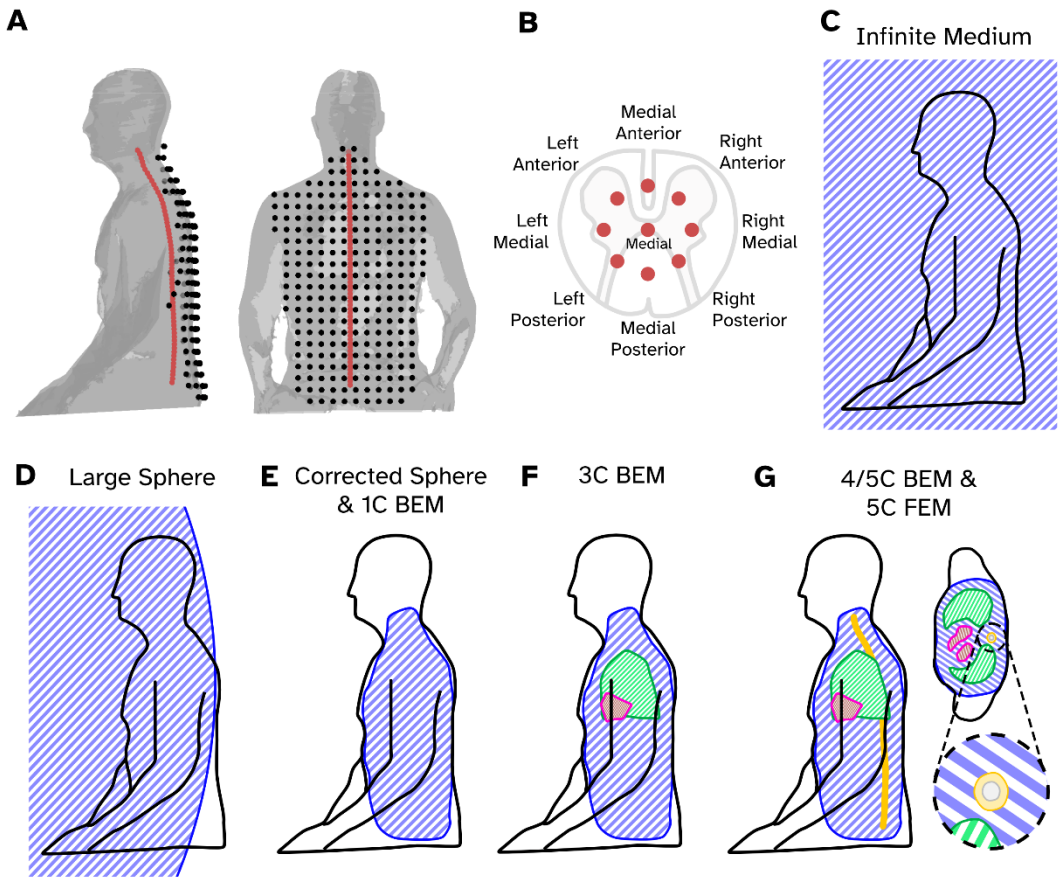

Figure 1 - Setup of the source, sensor and volume conductor models for the simulations. A) The sensor (black dots) and medial source locations (red dots) relative to a structural scan of the example participant (grey surface). B) The locations of 9 modelled source locations for a transverse "slice" of spinal cord, a cartoon slice of spinal cord has been superimposed to illustrate where these sources are sat. C-G) Cartoon diagrams showing how the main conductive boundary for each tested forward model (blue shaded area) is positioned. In addition to the main volume, sub domains representing the lungs (green), heart (red), spinal cord (grey) and vertebrae (yellow) and depicted. Panel G also includes a transverse slice through the chest to show the locations of the conductivity boundaries in more detail.

2.3 Model Evaluation

2.3.1 Direct comparison between lead field patterns

For a given forward model at each of the candidate source locations, three dipoles oriented along the cardinal axes were generated. For a given source and orientation we compared lead fields from all models with two metrics. First, for a pair of leadfield topography vectors l_a and l_b, the relative error is:

$$RE(l_a, l_b) = \frac{|l_a - l_b|}{|l_a| + |l_b|}, \qquad (1)$$

where $|l_a|$ represents the L2 norm of the lead field pattern l_a. Note that this metric, in contrast to other field comparison studies (Cao et al., 2022; Stenroos et al., 2014), is symmetric and bound between 0 and 1, where 0 is identical and 1 represents dissimilarity. The limitation of the relative error measure here is that when the error is high, we cannot disambiguate whether this is due to a global

gain error in the lead field or whether that the two are uncorrelated. We therefore also consider the correlation coefficient between l_a and l_b:

$$CC(l_a, l_b) = \frac{l_a - \overline{l_a}}{|l_a - \overline{l_a}|} \cdot \frac{l_b - \overline{l_b}}{|l_b - \overline{l_b}|}, \qquad (2)$$

where $\overline{l_a}$ is the mean of the vector l_a.

2.3.2 Decomposition of orientation sensitivity

Given we model current flow in all three cardinal directions for a given source, it is possible to determine which orientations we have sensitivity for a given volume conductor. For a triplet of field topographies $L = [l_x\ l_y\ l_z]$, where l_x, l_y and l_z are column vectors representing the field topographies of current flow in three orthogonal orientations from the same point in space, we can perform a singular value decomposition (SVD) of the matrix such that

$$L = U\Sigma V. \qquad (3)$$

The columns of U represent the each of the 3 normalised 'eigenfields', the diagonal elements of Σ represent the relative intensities of the eigenfields and the rows of V represent the orientation of the current flow of the corresponding eigenfields relative to the original coordinate frame.

3) Results

Figure 2 shows an example of a lead field topography generated with a finite element model. The source originates from approximately the T9 area of the spinal cord and the dipole has been oriented in each of the three cardinal orientations. For each lead field we plot each axis from the triaxial OPMs we simulated, with the Y-axis here defining the "axial" orientation (oriented normal to the plane of the screen). X (inferior-superior) and Z (left-right) correspond to sensitivity tangential the surface of the back. Looking first at a dipole oriented anterior to posterior (A-P) and right to left (R-L) we notice on the Y-axis channels we see their dipolar field patterns exhibit a similar pattern, but rotated by 45 degrees. But when looking at the tangential field patterns we notice that the L-R dipole has a distinct quadrupolar field pattern absent from the A-P oriented source as well as a peak field measured by a channel being approximately 5 times larger for the R-L source (2.5 fT/nAm for the R-L source vs. 0.4 fT/nAm for the A-P source). Furthermore, the channels with the most sensitivity to the R-L and S-I are tangentially oriented to the subject (sensing the field which is antiparallel to the current flow). The final observation is that the dipole oriented inferior to superior (I-S) has a maxima which is approximately 4 times larger than for the R-L oriented source (9.6 fT/nAm for the I-S source vs. 2.5 fT/nAm for the L-R source). On observing this result, we hypothesised this may be due to the conductivity and morphology of the bone compartment; current flow along the inferior-superior axis of the spine will be unattenuated compared to off-axis current flow. We investigate this further later in the results.

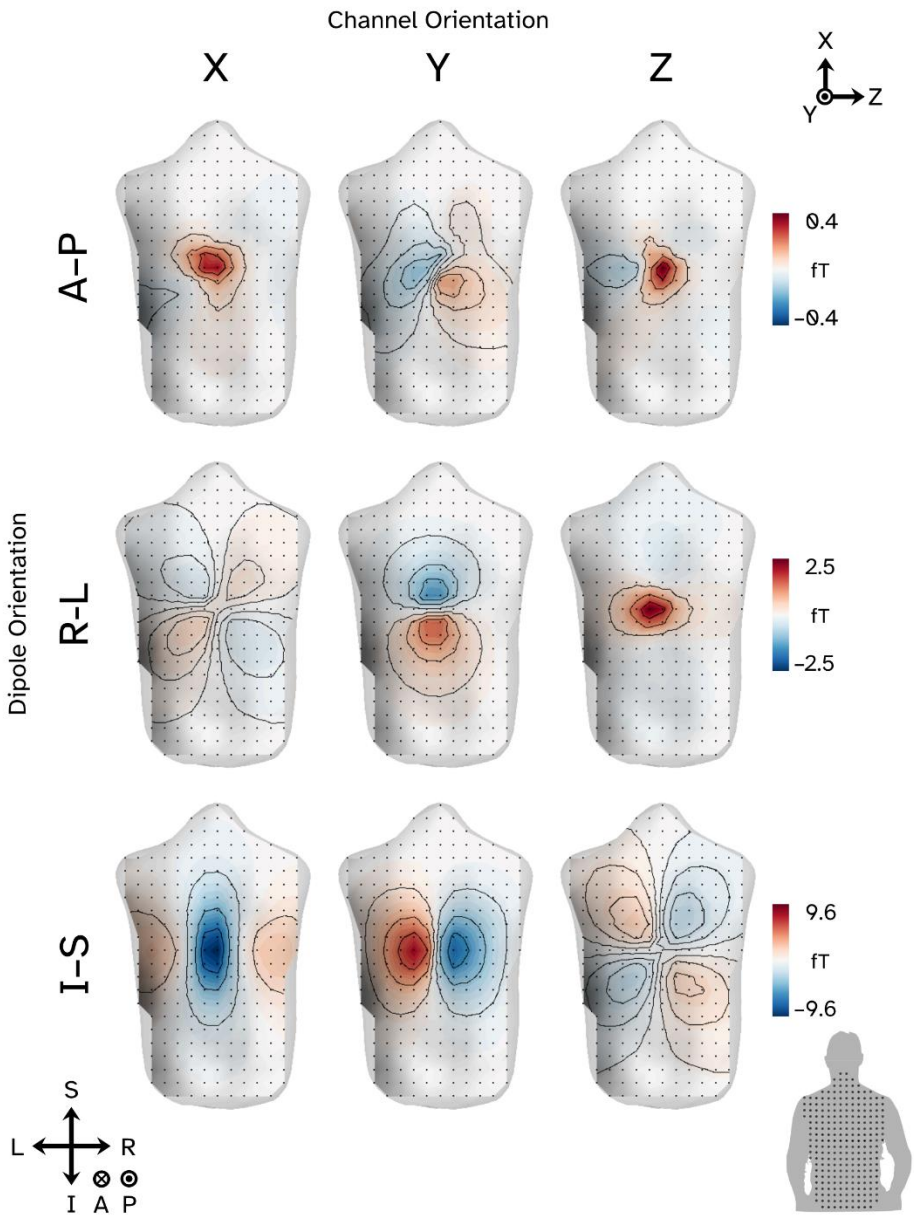

Figure 2 – Sensor level field topographies for a 1 nAm current dipole simulated in the thoracic region of the spine (approximately T9) when the sources are oriented along the anterior/posterior (A-P) axis of the body (top row), right/left (R-L) axis (middle row) and inferior/superior (I-S) axis (bottom row). The plots are sorted into channels with a common orientation in rows. X and Z (left and right columns) represent channels oriented tangential to the surface of the back whilst Y (middle column) represents the channels oriented normal to the back. Black dots represent sensor locations and black lines represent field contours to aid visualisation.

3.1 Direct comparisons between models and solutions

In Figure 3, we directly compare the field patterns produced by the 60 medial (c.f. Figures 1A-B) sources under different forward modelling assumptions to one another with our error and correlation metrics. Each element of Figure 3A is the median relative error between a pair of models when we include field topographies generated from source currents flowing in any of the three cardinal orientations. We see two distinct clusters of models with low error relative to each other. First are the conductive models which all contain bone (5c BEMs and FEM). Second are the bone-free numerical models (1c-4c BEMs), and then the three analytical solutions (infinite and spherical models) do not cluster with anything. Focusing on the correlation between models (Figure 3D), we see the majority of models show very high similarity to each other, with all the analytical models (1c BEM up to FEM) showing a median squared correlation of 0.95 or higher. To aid visualisation of the matrices we have plotted the errors and correlation between the FEM and all other models (Figure 3G), in other words just the final row or column of Figures 3A and 3D. We can see that relative to the FEM, the models containing bone (right of the dashed line in Fig. 3G) have a low error and high correlation, the bone-free numerical models (1c-4c BEM) have larger errors but still high correlation, finally the numerical models showing the largest errors and lowest correlations.

To distinguish whether there are any orientation specific differences between models, we have also plotted the error and correlation matrices for current flowing along the right-left axis (Figures 3B,E,H) and the inferior-superior axis (Figures 3C,F,I). Sources in the AP direction were omitted here as the field magnitudes are considerably (~20 times) smaller, but are available in the supplementary material. For right-left current flow, we see the relative error (Fig 3B) split into two clusters, the models containing bone and bone-free models. The correlations show high similarity for all realistically shaped models (Fig 3E), before falling for the large sphere and infinite models. With the two metrics overlaid (Fig 3H), we see the bone-free models (relative to the FEM) have large errors, but curiously high correlation – implying the field patterns are similar but overall gain has been affected. Sources oriented inferior-superior show overall low errors between models and high correlations (especially for any models realistically shaped such as the corrected sphere up to the FEM).

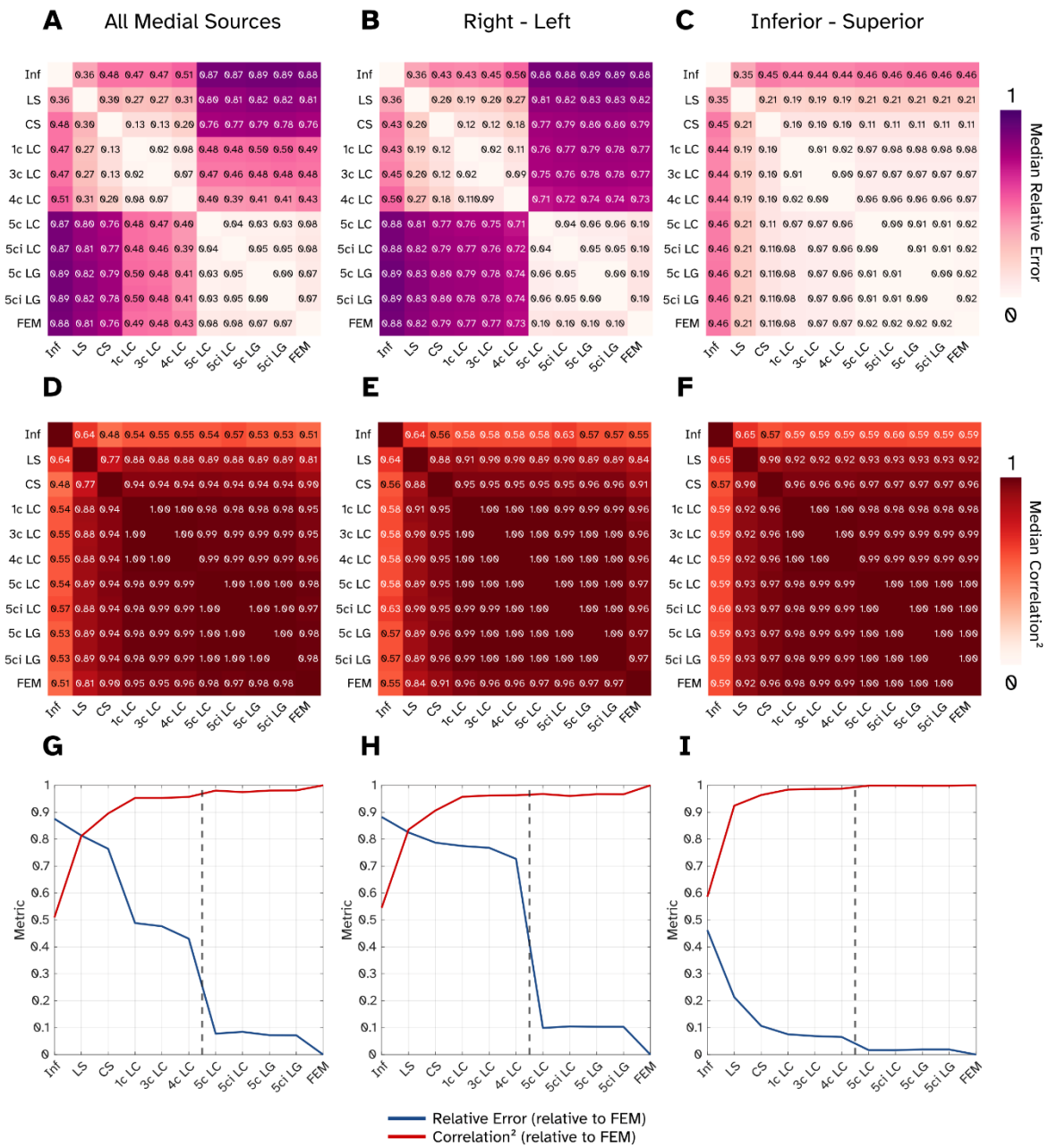

Figure 3 – Assessment of the similarities and differences between all 10 volume conductive modelling approaches when investigating only the medial sources. **A-C)** The median relative error between pairs of models represented in matrix form. Here errors are displayed when current flow is modelled in all three cardinal orientations (A), only sources oriented right-left (B) and inferior-superior (C). **D-F)** The median correlation coefficient (squared) between pairs of models for all orientations (D), right-left (E) and inferior-superior (F). **G-I)** Both the relative and correlations plotted, but this time between the Finite Element Model (FEM) and all other models for all orientations (G) right-left (H) and inferior-superior (I). Black dashed line shows the boundary between models containing bone (right of line) and not.

3.2 Field decomposition reveals orientation-specific sensitivity for bone models

For each source in the medial location along the spinal cord, we performed SVD on each triplet of lead fields for a given location to determine which principal orientations of current flow each conductive model is sensitive to. Figure 4A and 4B show examples of the first two eigenfields for a conductive model with includes no bone (1c LC; Fig. 4A) and with bone (5c LC. Fig 4B). These two models were chosen as they employ the same numerical approach to solve the forward problem (linear collocation BEM). The eigenfield topographies plotted have been un-normalised (i.e. we are plotting the columns of $U\Sigma$) to visualise their relative intensities. In the bone-free 1c LC model (Fig. 4A), the first component represents current flow oriented along the right-left axis. In other words, when all directions of current flow are equally represented in the cord, the predominant picture at the sensor level is that of current flowing left-right. The second component, by contrast, would correspond to current flow in the superior-inferior direction. The two components have similar intensities (the ratio between the two eigenvalues contained in Σ is 1.07). The third eigenfield (not pictured) represents a current flow in the anterior-posterior direction and is (as expected) considerably smaller than the other two components (eigenvalue 3 is 27 times smaller than eigenvalue 1). If we include a bone component in our conductive modelling (Fig. 4B) we observe two differences, first the preferential order of the orientations is now superior-inferior followed by left-right. Second the intensity of the second component is considerably smaller (ratio of eigenvalue 1 and eigenvalue 2 is 6.50).

We quantify these differences in orientation sensitivity for all models across all medial sources in Figures 4C-D. Here, the source IDs are such that lower IDs represent the inferior/lumbar portion of the spinal cord and superior portions have higher IDs. Figure 4C shows the ratio between the first and second eigenvalues at each medial point of the spinal cord. Between sources 10-50 (where we think the whole field topography is adequately sampled) the bone-free models (cooler coloured lines) have a ratio of approximately 1, whereas the models with bone (warmer colours) have a much higher ratio (min: 5.37, max: 7.80). Figure 4D shows the angle between the inferior-superior axis and the orientation of the source that would produce the dominant eigenfield. For example, in Figure 4A, the dominant current flow is left-right and therefore, there is a 90 degree angle to the anterior-superior direction; in 4B by contrast the angle is zero. Figure 4D shows that for bone free models, the dominant field pattern is often due to the source component in the left-right direction. Adding additional compartments (3c-4c LC) shows that these tissues start to dictate the primary sensitivity axis (as the first two eigenmodes have similar amplitudes). For the 3c LC model, we see that the lungs and heart affect sources with IDs 30-50, with the primary orientation rotating to be nearer the IS axis rather than the RL axis. Adding the 4th compartment (white matter of the spinal cord) shows the primary sensitivity axis is closer to the curvature of the spine (dashed magenta line). However, in both these cases, the first and second eigenfields are of similar intensity and so this preferential orientation discussion is a moot point. As soon as we add the bone into the models, we see that the primary eigenfield is oriented along the direction of the spinal curvature. Combined with the fact the first eigenfield is several factors larger than the second, the bone appears to give maximal sensitivity along the cord's superior-inferior axis, at the expense of all other orientations.

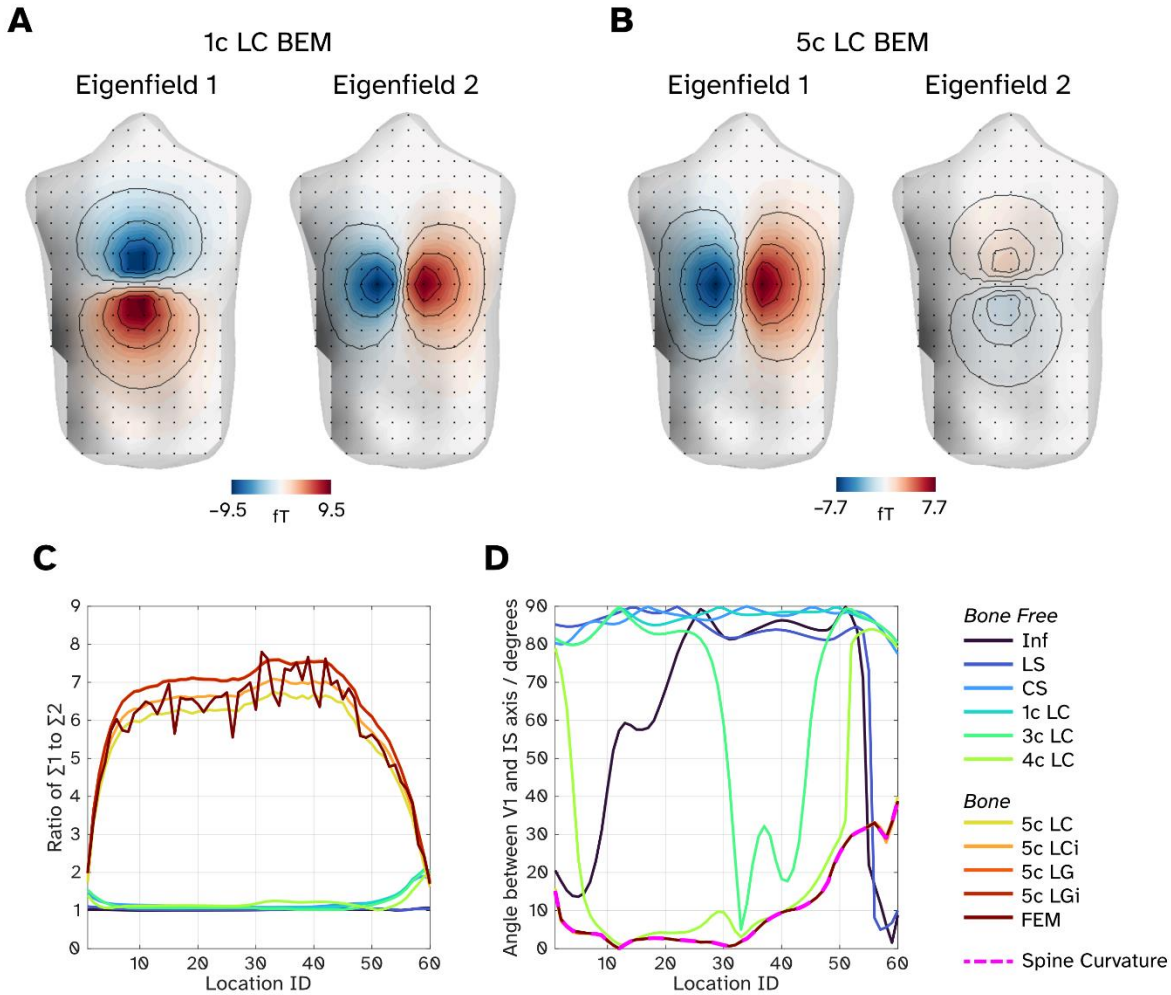

Figure 4 – Analysis of sensitivity to the orientation of current flow but modelling source currents in all three cardinal axes and decomposing the field topographies **A)** First two eigenfields for a source located approximately at T9 for a 1-comparment model solved with a linear collocation BEM, showing similar sensitivity in the first two primary axes. **B)** First two eigenfields for the same source but using a 5-compartment model solved with a linear collocation BEM, revealing one dominant component along the inferior-superior axis. **C)** Quantification of the relative strengths of the first two eigenfields for a given model and source by measuring the ration of the two associated eigenvalues. Lower location ID indexes the inferior-superior (lower-higher values) position along the cord. **D)** The angle between the inferior-superior axis and the first eigenfield, the magenta dashed line represents the angle between the spine and the inferior-superior axis.

3.3 Bone-based models may offer better lateral source separation

Finally, we compare the field topographies of the left medial to the right medial sources for a given slice of spinal cord. The motivation here is to determine if the field topographies offer enough separability between the two sources to determine the lateralisation of a current, so we are looking for higher relative errors and lower correlations between a pair of topographies. Here, we specifically compare current flow oriented along the curvature of the spine to reduce our comparisons down from 3 field topographies per source to 1. Figure 5A shows boxplots representing the relative errors between pairs of field topographies, with each jittered point representing a pair of sources. Increasing the complexity of bone-free models (Inf to 4c LC) lead to larger relative errors between the left and right sources, but it is the introduction of the bone compartment which leads the largest increase of errors between sources. Given the field topographies are of a pair of sources should be approximately equal in magnitude, we would expect the correlations between fields to be inversely proportional to the errors. This is what we observe in Figure 5B, where bone-based models tend to have lower squared-correlations between sources. To illustrate one case, Figures 5C and 5D show the modelled field topography for a pair of sources in the T9 location and the difference between patterns for a bone-free (1c LC; Fig 5C) and bone (5c LC; Fig 5D) models. The 1c LC model generates field topographies where the extreme fields at the poles are almost equal in magnitude (9.6 fT/nAm v -9.2 fT/nAm, 95% for the left medial source) whereas the bone introduces an asymmetry (7.0 fT/nAm v -8.3 fT/nAm, 84% for the left medial source). This asymmetry in the field patterns and intensities lead to greater differences (or improved discriminability) between the two sources and thus larger relative errors and lower correlations.

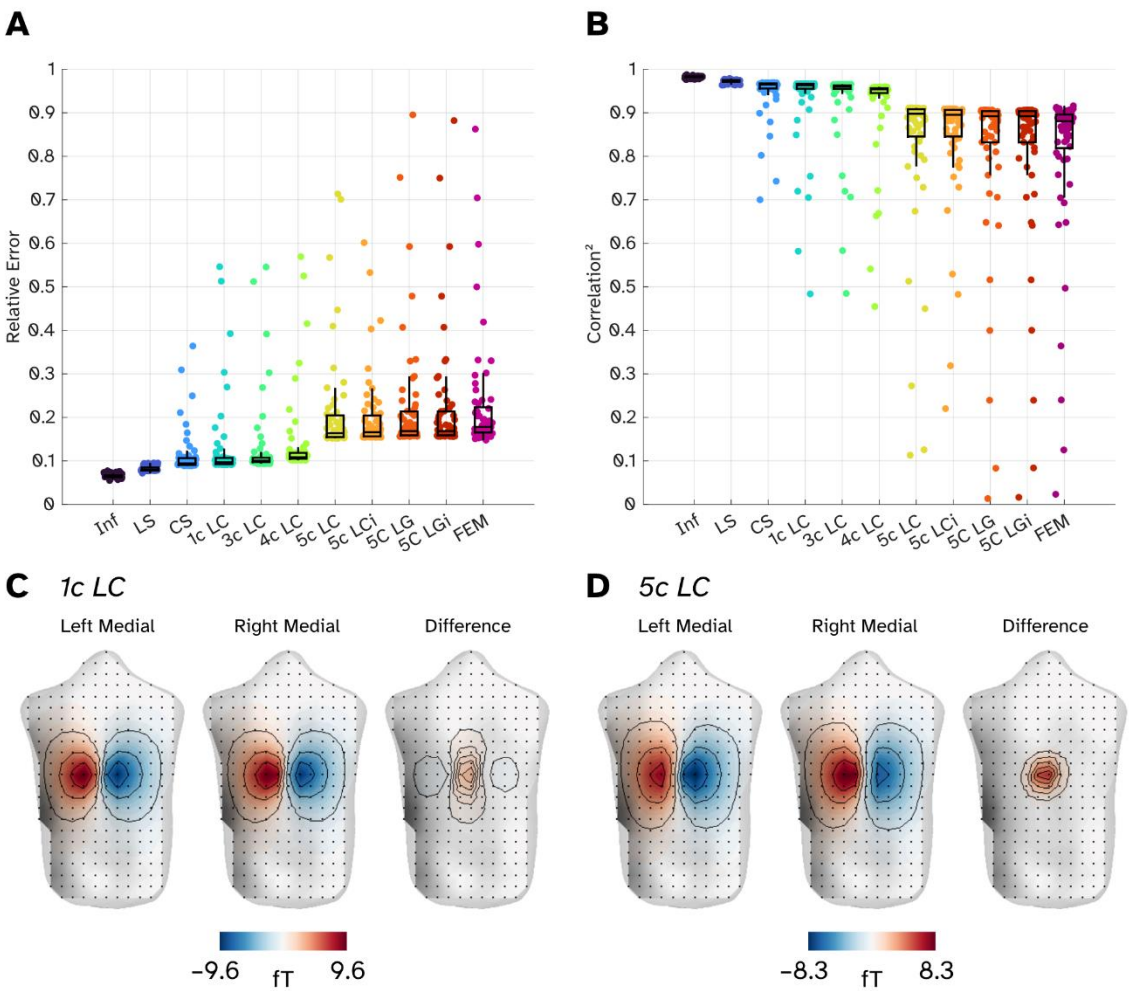

Figure 5 – The similarity and differences of field topographies from lateralised sources in the spinal cord. **A)** Relative errors between pairs of sources in a given slice of spinal cord (left medial and right medial sources). Individual points represent a pair of sources whilst boxplots show the median errors across the entire spinal cord. **B)** Squared correlation coefficients between pairs of sources. **C)** Visualisation of the field topographies for a pair of 1 nAm source currents in the T9 region of the spine and the difference between them for a bone free model (1c LC BEM). **D)** Field topographies for two lateral sources in T9 for a volume conductor containing bone (5c LC BEM).

4) Discussion

We have tested different forward models describing how current flow in the spinal cord manifests as magnetic fields outside the torso. We tested these for elements of current flow situated from cervical to lumbar regions of the spinal cord oriented in three directions.

We found that most conductive models can approximate the field topography for a source current oriented along the inferior-superior axis of the body (assuming some attempt to model the torso boundary has been implemented). The infinite homogenous medium model generates lead fields which are the most distinct from any other volume conductor tested but, perhaps surprisingly, a large sphere compared well to realistically shaped torsos. Our assumption is that by moving the origin so far forward, all dipoles oriented along the inferior-superior and left-right axes are considered tangential sources (relative to the sphere) origin and so are preserved. In fact, if one continued to move the origin an infinite distance in front of the subject one would converge on a half-space model (Sarvas, 1987), where the conductive model approximates into a flat plane representing the subject's back. The corrected sphere was the most similar of the three analytical models to the numerical methods (BEMs and FEM). However, we note that the implementation of the corrected sphere here uses a basis set which does not tolerate the sensors being so close to the conductive boundary (Nolte, 2003), and so produces artefactual field patterns (see supplementary material). So, if one wanted the most rudimentary volume conductor to perform a basic source analysis along the inferior-superior axis, a single compartment boundary element model could be the safest recommendation.

Our main finding was that the inclusion of bone wrapped around our spinal cord affects the field topographies in non-trivial ways. First, we found that the sensitivity to different orientations of current was driven primarily by whether bone was included in the volume conductor. Bone-free models had equal sensitivity to sources oriented along the superior-inferior and left-right axes, while the bone-inclusive models had a single preferential axis: along the curvature of the spinal cord. The second component (left-right oriented) is attenuated in magnitude in our simulations by as much as 5- to 8-fold, depending on how well sampled the source is by the sensors and which forward solution was implemented. The field topographies of left-right oriented sources produced were similar in pattern across all numerical models (BEMs and FEM), implying that in our simple model of the vertebrae, the bone essentially acts as a "global" attenuator of the sensitivity to current flow off-axis to the inferior-superior axis of the spine. When separating out the effects primary and secondary current flow on the magnetic field, we see that the secondary currents generates an almost equal and opposing field to the primary currents for transverse oriented current flow (supplementary material). With a realistic spinal column geometry, this effect may be even more complicated to characterise than merely a simple scaling of the field strength. Whilst we note that our bone model was not anatomically accurate (vertebrae are not rotationally symmetric, discrete entities, and vary in size), we would still expect there to be an orientation dependent effect with a realistic geometry. Future work could investigate realistic anatomies.

Our second bone-based model observation is how the inclusion of bone allows for theoretically better separation of sources in the same transverse plane of the spinal cord. We found that sources placed 8 mm apart in the same transverse slice of spinal cord had associate field topographies which were more dissimilar if bone was incorporated. In part, this was due to how poles of the field topography were distorted by bone. The pole proximal to the bone walls attenuated more than the other. We note that the similarity in field patterns based on correlations was still very high (around 90 % variance explained by each other) in our theoretical sensor array, but with methods available to optimise sensor

sampling (Beltrachini et al., 2021; Iivanainen et al., 2021; Tierney et al., 2020) we may reduce the correlations further. The use of bone-based models may allow for direct confirmation of source laterality in the spinal cord, something only fMRI has demonstrated (non-invasively) so far (Dabbagh et al., 2024; Sprenger et al., 2012).

These findings motivate more work into the modelling of the bone around the spinal cord. This would allow one to more accurately characterise spinal cord activity at the source level; otherwise orientation-related gain errors will result in the poor estimation of off-axis current flow in the spinal cord (from for example, integration from spinal interneurons; Deska-Gauthier and Zhang, 2019). The need for bone modelling implies that the location of the spinal cord should be known *a priori* to facilitate this. Generative modelling approaches to determine the location of the spinal cord from the sensor data alone would become too computationally expensive if we must solve a complex BEM or FEM volume conductor iteratively for a wide range of possible source spaces. Rather, it would be simpler to determine from structural imaging. SQUID-based MSG systems have taken an X-ray of the participant in situ of the sensors (Sakaki et al., 2020; Sumiya et al., 2017; Ushio et al., 2019) to determine their source space. However, this would not be possible for OPM-based systems as it would risk damaging the sensors. Imaging the spine and torso with (for example) MRI is commonplace (Valošek and Cohen-Adad, 2024) so could be employed. However, from a practical perspective this is by no means a trivial thing to do. Between the MRI and the MSG unless carefully controlled, the posture of the participant will change, and so too will the position of the spinal cord (and the vertebrae), undermining this complexity by not knowing exactly where the sensors are with respect to the sources of interest – something that increasingly accurate forward models cannot tolerate well (Cao et al., 2022; Duque-Muñoz et al., 2019).

In summary the inclusion of the bone in volume conductors for source currents in the spinal cord generates features which cannot trivially be emulated in the absence of bone, and so will be essential to maximise the quality of the source analysis MSG can provide. With this in mind, we can now focus on optimizing sensor placement for denoising recordings and inverse modelling in the future.

Acknowledgments

GCO is funded through an UKRI Frontier Research Grant [EP/X023060/1] and acknowledges EPSRC [EP/T001046/1] funding from the Quantum Technology hub in sensing and timing (sub-award QTPRF02). MES is supported by a Wellcome Technology Development grant [223736/Z/21/Z]. MS supported by the UZH Global Strategy and Partnerships Fund Scheme. SM was supported by an EPSRC Healthcare Impact Partnership Grant [EP/V047264/1] and acknowledges support from the Federal Commission for Scholarships for Foreign Students for the Swiss Government Excellence Scholarship (ESKAS No. 2024.0251). This research was supported by the Discovery Research Platform for Naturalistic Neuroimaging funded by Wellcome [226793/Z/22/Z].

Data availability

Code for generation of the results can be found at https://github.com/georgeoneill/study-spinevol. Supporting toolbox for the generation of the volume conductors and solvers can be found at https://github.com/fil-opmeg/torso_tools. The linear Galerkin BEM solver is only available for Aalto University collaborators – please contact Matti Stenroos to request access.

References

Adachi, Y., Kawabata, S., 2024. SQUID magnetoneurography: an old-fashioned yet new tool for noninvasive functional imaging of spinal cords and peripheral nerves. Front. Med. Technol. 6. https://doi.org/10.3389/fmedt.2024.1351905

Akaza, M., Kawabata, S., Ozaki, I., Miyano, Y., Watanabe, T., Adachi, Y., Sekihara, K., Sumi, Y., Yokota, T., 2021. Noninvasive measurement of sensory action currents in the cervical cord by magnetospinography. Clin. Neurophysiol. 132, 382–391. https://doi.org/10.1016/j.clinph.2020.11.029

Beltrachini, L., von Ellenrieder, N., Eichardt, R., Haueisen, J., 2021. Optimal design of on-scalp electromagnetic sensor arrays for brain source localisation. Hum. Brain Mapp. 42, 4869–4879. https://doi.org/10.1002/hbm.25586

Brookes, M.J., Boto, E., Rea, M., Shah, V., Osborne, J., Holmes, N., Hill, R.M., Leggett, J., Rhodes, N., Bowtell, R., 2021. Theoretical advantages of a triaxial optically pumped magnetometer magnetoencephalography system. NeuroImage 236, 118025. https://doi.org/10.1016/j.neuroimage.2021.118025

Cao, F., An, N., Wang, W., Xu, W., Li, W., Wang, C., Xiang, M., Gao, Y., Ning, X., 2022. Effects of Different Head Models in Wearable OPM-MEG. IEEE Trans. Instrum. Meas. 71, 1–10. https://doi.org/10.1109/TIM.2022.3192287

Chander, B.S., Deliano, M., Azañón, E., Büntjen, L., Stenner, M.-P., 2022. Non-invasive recording of high-frequency signals from the human spinal cord. NeuroImage 253, 119050. https://doi.org/10.1016/j.neuroimage.2022.119050

Dabbagh, A., Horn, U., Kaptan, M., Mildner, T., Müller, R., Lepsien, J., Weiskopf, N., Brooks, J.C.W., Finsterbusch, J., Eippert, F., 2024. Reliability of task-based fMRI in the dorsal horn of the human spinal cord. Imaging Neurosci. 2, 1–27. https://doi.org/10.1162/imag_a_00273

Deska-Gauthier, D., Zhang, Y., 2019. The functional diversity of spinal interneurons and locomotor control. Curr. Opin. Physiol., Motor Control Systems 8, 99–108. https://doi.org/10.1016/j.cophys.2019.01.005

Duque-Muñoz, L., Tierney, T.M., Meyer, S.S., Boto, E., Holmes, N., Roberts, G., Leggett, J., Vargas-Bonilla, J.F., Bowtell, R., Brookes, M.J., López, J.D., Barnes, G.R., 2019. Data-driven model optimization for optically pumped magnetometer sensor arrays. Hum. Brain Mapp. 40, 4357–4369. https://doi.org/10.1002/hbm.24707

Hamalainen, M.S., Sarvas, J., 1989. Realistic conductivity geometry model of the human head for interpretation of neuromagnetic data. IEEE Trans. Biomed. Eng. 36, 165–171. https://doi.org/10.1109/10.16463

Hashimoto, J., Kawabata, S., Sasaki, T., Hoshino, Y., Sekihara, K., Adachi, Y., Watanabe, T., Miyano, Y., Mitani, Y., Sato, S., Kim, S., Yoshii, T., Okawa, A., 2022. Assessment of thoracic spinal cord electrophysiological activity through magnetoneurography. Clin. Neurophysiol. 133, 39–47. https://doi.org/10.1016/j.clinph.2021.09.023

Iivanainen, J., Mäkinen, A.J., Zetter, R., Stenroos, M., Ilmoniemi, R.J., Parkkonen, L., 2021. Spatial sampling of MEG and EEG based on generalized spatial-frequency analysis and optimal design. NeuroImage 245, 118747. https://doi.org/10.1016/j.neuroimage.2021.118747

Imajo, Y., Kanchiku, T., Suzuki, H., Nishida, N., Funaba, M., Taguchi, T., Sakai, T., 2021. Assessment of spinal cord relative vulnerability in C4–C5 compressive cervical myelopathy using multi-modal spinal cord evoked potentials and neurological findings. J. Spinal Cord Med. 44, 541–548. https://doi.org/10.1080/10790268.2019.1617920

Kawabata, S., Komori, H., Mochida, K., Harunobu, O., Shinomiya, K., 2002. Visualization of Conductive Spinal Cord Activity Using a Biomagnetometer. Spine 27, 475.

Mardell, L.C., Spedden, M.E., O'Neill, G.C., Tierney, T.M., Timms, R.C., Zich, C., Barnes, G.R., Bestmann,

S., 2024. Concurrent spinal and brain imaging with optically pumped magnetometers. J. Neurosci. Methods 110131. https://doi.org/10.1016/j.jneumeth.2024.110131

Medani, T., Garcia-Prieto, J., Tadel, F., Antonakakis, M., Erdbrügger, T., Höltershinken, M., Mead, W., Schrader, S., Joshi, A., Engwer, C., Wolters, C.H., Mosher, J.C., Leahy, R.M., 2023. Brainstorm-DUNEuro: An integrated and user-friendly Finite Element Method for modeling electromagnetic brain activity. NeuroImage 267, 119851. https://doi.org/10.1016/j.neuroimage.2022.119851

Nielsen, J.B., 2016. Human Spinal Motor Control. Annu. Rev. Neurosci. 39, 81–101. https://doi.org/10.1146/annurev-neuro-070815-013913

Nielsen, J.B., 2004. Sensorimotor integration at spinal level as a basis for muscle coordination during voluntary movement in humans. J. Appl. Physiol. 96, 1961–1967. https://doi.org/10.1152/japplphysiol.01073.2003

Nolte, G., 2003. The magnetic lead field theorem in the quasi-static approximation and its use for magnetoencephalography forward calculation in realistic volume conductors. Phys. Med. Biol. 48, 3637–3652. https://doi.org/10.1088/0031-9155/48/22/002

O'Neill, G.C., Seymour, R.A., Mellor, S., Alexander, N., Tierney, T.M., Bernachot, L., Hnazaee, M.F., Spedden, M.E., Timms, R.C., Bestmann, S., Brookes, M.J., Barnes, G.R., 2023. Combining video telemetry and wearable MEG for naturalistic imaging (preprint). Neuroscience. https://doi.org/10.1101/2023.08.01.551482

Oosterom, A. van, Oostendorp, T.F., 2004. ECGSIM: an interactive tool for studying the genesis of QRST waveforms. Heart 90, 165–168. https://doi.org/10.1136/hrt.2003.014662

Prestor, B., Žgur, T., Dolenc, V.V., 1991. Subpially recorded cervical spinal cord evoked potentials in syringomyelia. Electroencephalogr. Clin. Neurophysiol. Potentials Sect. 80, 155–158. https://doi.org/10.1016/0168-5597(91)90153-O

Rejc, E., Angeli, C.A., Atkinson, D., Harkema, S.J., 2017. Motor recovery after activity-based training with spinal cord epidural stimulation in a chronic motor complete paraplegic. Sci. Rep. 7, 13476. https://doi.org/10.1038/s41598-017-14003-w

Rhodes, N., Rea, M., Boto, E., Rier, L., Shah, V., Hill, R.M., Osborne, J., Doyle, C., Holmes, N., Coleman, S.C., Mullinger, K., Bowtell, R., Brookes, M.J., 2023. Measurement of Frontal Midline Theta Oscillations using OPM-MEG. NeuroImage 271, 120024. https://doi.org/10.1016/j.neuroimage.2023.120024

Sakaki, K., Hoshino, Y., Kawabata, S., Adachi, Y., Watanabe, T., Sekihara, K., Ishii, S., Tomori, M., Tomizawa, S., Enomoto, M., Okawa, A., 2020. Evaluation of neural activity by magnetospinography with 3D sensors. Clin. Neurophysiol. 131, 1252–1266. https://doi.org/10.1016/j.clinph.2020.02.025

Sarvas, J., 1987. Basic mathematical and electromagnetic concepts of the biomagnetic inverse problem. Phys. Med. Biol. https://doi.org/10.1088/0031-9155/32/1/004

Schrader, S., Westhoff, A., Piastra, M.C., Miinalainen, T., Pursiainen, S., Vorwerk, J., Brinck, H., Wolters, C.H., Engwer, C., 2021. DUNEuro—A software toolbox for forward modeling in bioelectromagnetism. PLOS ONE 16, e0252431. https://doi.org/10.1371/journal.pone.0252431

Shackleton, C., Samejima, S., Williams, A.M., Malik, R.N., Balthazaar, S.J., Alrashidi, A., Sachdeva, R., Elliott, S.L., Nightingale, T.E., Berger, M.J., Lam, T., Krassioukov, A.V., 2023. Motor and autonomic concomitant health improvements with neuromodulation and exercise (MACHINE) training: a randomised controlled trial in individuals with spinal cord injury. BMJ Open 13, e070544. https://doi.org/10.1136/bmjopen-2022-070544

Spedden, M., O'Neill, G., Tierney, T., West, T., Schmidt, M., Mellor, S., Farmer, S.F., Bestmann, S., Barnes, G., 2024. Towards non-invasive imaging through spinal-cord generated magnetic fields. Front. Med. Technol. 6. https://doi.org/10.3389/fmedt.2024.1470970

Sprenger, C., Eippert, F., Finsterbusch, J., Bingel, U., Rose, M., Büchel, C., 2012. Attention Modulates

Spinal Cord Responses to Pain. Curr. Biol. 22, 1019–1022. https://doi.org/10.1016/j.cub.2012.04.006

Steele, A.G., Faraji, A.H., Contreras-Vidal, J.L., 2024. Electrospinography for non-invasively recording spinal sensorimotor networks in humans. J. Neural Eng. 20, 066043. https://doi.org/10.1088/1741-2552/ad1782

Stenroos, M., Hunold, A., Haueisen, J., 2014. Comparison of three-shell and simplified volume conductor models in magnetoencephalography. NeuroImage 94, 337–348. https://doi.org/10.1016/j.neuroimage.2014.01.006

Stenroos, M., Mäntynen, V., Nenonen, J., 2007. A Matlab library for solving quasi-static volume conduction problems using the boundary element method. Comput. Methods Programs Biomed. 88, 256–263. https://doi.org/10.1016/j.cmpb.2007.09.004

Stenroos, M., Nummenmaa, A., 2016. Incorporating and Compensating Cerebrospinal Fluid in Surface-Based Forward Models of Magneto- and Electroencephalography. PloS One 11, e0159595. https://doi.org/10.1371/journal.pone.0159595

Stenroos, M., Sarvas, J., 2012. Bioelectromagnetic forward problem: isolated source approach revis(it)ed. Phys. Med. Biol. 57, 3517. https://doi.org/10.1088/0031-9155/57/11/3517

Stroman, P.W., Wheeler-Kingshott, C., Bacon, M., Schwab, J.M., Bosma, R., Brooks, J., Cadotte, D., Carlstedt, T., Ciccarelli, O., Cohen-Adad, J., Curt, A., Evangelou, N., Fehlings, M.G., Filippi, M., Kelley, B.J., Kollias, S., Mackay, A., Porro, C.A., Smith, S., Strittmatter, S.M., Summers, P., Tracey, I., 2014. The current state-of-the-art of spinal cord imaging: Methods. NeuroImage 84, 1070–1081. https://doi.org/10.1016/j.neuroimage.2013.04.124

Sumiya, S., Kawabata, S., Hoshino, Y., Adachi, Y., Sekihara, K., Tomizawa, S., Tomori, M., Ishii, S., Sakaki, K., Ukegawa, D., Ushio, S., Watanabe, T., Okawa, A., 2017. Magnetospinography visualizes electrophysiological activity in the cervical spinal cord. Sci. Rep. 7, 2192. https://doi.org/10.1038/s41598-017-02406-8

Tierney, T.M., Mellor, S., O'Neill, G.C., Holmes, N., Boto, E., Roberts, G., Hill, R.M., Leggett, J., Bowtell, R., Brookes, M.J., Barnes, G.R., 2020. Pragmatic spatial sampling for wearable MEG arrays. Sci. Rep. 10, 21609. https://doi.org/10.1038/s41598-020-77589-8

Tierney, T.M., Mellor, S., O'Neill, G.C., Timms, R.C., Barnes, G.R., 2022. Spherical harmonic based noise rejection and neuronal sampling with multi-axis OPMs. NeuroImage 258, 119338. https://doi.org/10.1016/j.neuroimage.2022.119338

Tierney, T.M., Seedat, Z., St Pier, K., Mellor, S., Barnes, G.R., 2024. Adaptive multipole models of optically pumped magnetometer data. Hum. Brain Mapp. 45, e26596. https://doi.org/10.1002/hbm.26596

Umeda, T., Isa, T., Nishimura, Y., 2022. Temporal dynamics of the sensorimotor convergence underlying voluntary limb movement. Proc. Natl. Acad. Sci. 119, e2208353119. https://doi.org/10.1073/pnas.2208353119

Ushio, S., Hoshino, Y., Kawabata, S., Adachi, Y., Sekihara, K., Sumiya, S., Ukegawa, D., Sakaki, K., Watanabe, T., Hasegawa, Y., Okawa, A., 2019. Visualization of the electrical activity of the cauda equina using a magnetospinography system in healthy subjects. Clin. Neurophysiol. 130, 1–11. https://doi.org/10.1016/j.clinph.2018.11.001

Valošek, J., Cohen-Adad, J., 2024. Reproducible Spinal Cord Quantitative MRI Analysis with the Spinal Cord Toolbox. Magn. Reson. Med. Sci. 23, 307–315. https://doi.org/10.2463/mrms.rev.2023-0159

Vorwerk, J., Cho, J.-H., Rampp, S., Hamer, H., Knösche, T.R., Wolters, C.H., 2014. A guideline for head volume conductor modeling in EEG and MEG. NeuroImage 100, 590–607. https://doi.org/10.1016/j.neuroimage.2014.06.040